Tokamak magnetic field lines described by simple maps

Dedicated to Professor Celso Grebogi on the occasion of his 60th birthday

J.S.E. Portela[1], I.L. Caldas[1], and R.L. Viana[2,a]

[1] Instituto de Física, Universidade de São Paulo, Caixa Postal 66318, 05315-970 São Paulo, SP, Brazil
[2] Departamento de Física, Universidade Federal do Paraná, Caixa Postal 19081, 81531-990 Curitiba, Paraná, Brazil

Abstract. The magnetic field line structure in a tokamak can be obtained by direct numerical integration of the field line equations. However, this is a lengthy procedure and the analysis of the solution may be very time-consuming. Otherwise we can use simple two-dimensional, area-preserving maps, obtained either by approximations of the magnetic field line equations, or from dynamical considerations. These maps can be quickly iterated, furnishing solutions that mirror the ones obtained from direct numerical integration, and which are useful when long-term studies of field line behavior are necessary (e.g. in diffusion calculations). In this work we focus on a set of simple tokamak maps for which these advantages are specially pronounced.

1 Introduction

Tokamaks are the most promising devices for the magnetic confinement of fusion plasmas [1]. The stability of this confinement is an important problem in which the magnetic field line configuration plays a fundamental role – both by strongly influencing the transport that arises from fine scale turbulence [2] and by being the leading order approximation to the particle flux since charged particles tend to follow the magnetic field lines. Magnetic field lines are, in general, orbits of Hamiltonian systems of one-and-a-half degrees of freedom which are, provided the time-like coordinate is periodic, equivalent to two-dimensional area-preserving maps [3]. Consequently we can use such maps to describe the toroidal magnetic configurations of plasmas confined in tokamaks, what is particularly tailored for interpreting phenomena in the nonlinear dynamics framework.

The tokamak map trajectories can be obtained by directly integrating the field line differential equations, but that is a time-consuming calculation which may not be appropriate for studying long-term behavior of field lines, markedly transport properties. A more exact tokamak map could be obtained from the magnetohydrodynamical equations containing relatively few approximations, but this procedure would require numerical calculation of the functions in the map, what would take as much time as the integration of the magnetohydrodynamical equations themselves [4]. Therefore approximate maps have to be considered if one wants to have the advantage of much shorter computation times. Tokamak simple maps can result from physical considerations and mathematical approximations applied to the field line equations, or even be *ad hoc* maps whose suitability is based on the qualitative and quantitative agreement

---

[a] e-mail: `viana@fisica.ufpr.br`

with the physical situation they describe. These approximate maps may present different levels of sophistication and represent the tokamak magnetic field line structure with various degrees of accuracy. In this work we consider some simple maps proposed to investigate the fundamental features of the tokamak magnetic field line dynamics. Some of these maps have been introduced by the authors and their collaborators over the last fifteen years.

The paper is organized as follows: in section 2, we introduce basic concepts, including tokamak geometry, fundamental equations, and dynamical characteristics of two-dimensional maps. In section 3, we present the standard map and the standard non-twist map, stressing their general features. Section 4 deals with maps proposed to study the chaotic field lines due to an ergodic limiter. In section 5, we outline test models proposed by Balescu and co-workers, namely the tokamap and its non-twist version, the revtokamap. Section 6 treats maps used to study the field line structure due to divertors. We leave our conclusions to section 7.

2 Magnetic field lines in a tokamak

The tokamak toroidal geometry is essentially characterized by its major radius, R_0, which defines the circular magnetic axis around the symmetry axis of the torus, and its minor radius, b, measured from the magnetic axis. The angle measured from the major radius is the *toroidal angle*, ϕ, and the one from the minor radius is the *poloidal angle*, θ. The radius r, varying from the magnetic axis ($r = 0$) to the tokamak wall ($r = b$), labels a set of nested tori, which ideally correspond to the equilibrium magnetic flux surfaces. The main magnetic field of a tokamak has toroidal and poloidal components which are generated by external poloidal coils and the plasma current, respectively [1]. In addition to this equilibrium field, perturbative resonant fields can be added with many purposes, for example to control plasma-wall interactions [5–8]. The perturbative resonant fields are usually created by externally applied electric currents, like in divertors and ergodic magnetic limiters. The bigger the tokamak aspect ratio, R_0/b, the better is the approximation of the tokamak vessel by a periodic cylinder of length $2\pi R_0$, where the magnetic axis is parameterized by the coordinate $z = R_0\phi$ [1]. In this case the equilibrium toroidal field, B_ϕ, is nearly uniform and hence the toroidal effect can be treated as a perturbative factor or even neglected in a first approximation. Accordingly, a point in the tokamak is determined by its cylindrical coordinates (r, θ, z), sketched in Fig. 1. The poloidal curvature can also be neglected when considering regions close to the tokamak wall, where it turns out not to influence results in a noticeable way. In such approximation a rectangular coordinate system can be used: $x' = b\theta$ and $y' = b - r$ [9]. In these coordinates the tokamak wall is the line segment $y' = 0$, extending from $x' = 0$ to $2\pi b$. In the following we shall use the normalized coordinates $x = x'/(2\pi b)$ and $y = y'/b$ (or $y = r/b$) unless stated otherwise.

By definition, magnetic field lines are parallel to the field at each point, thus, **dl** being the line element, for a given equilibrium magnetic field, **B**, the field lines are determined by **B** × **dl** = 0. The integration of these equations gives the magnetic field lines trajectories but,
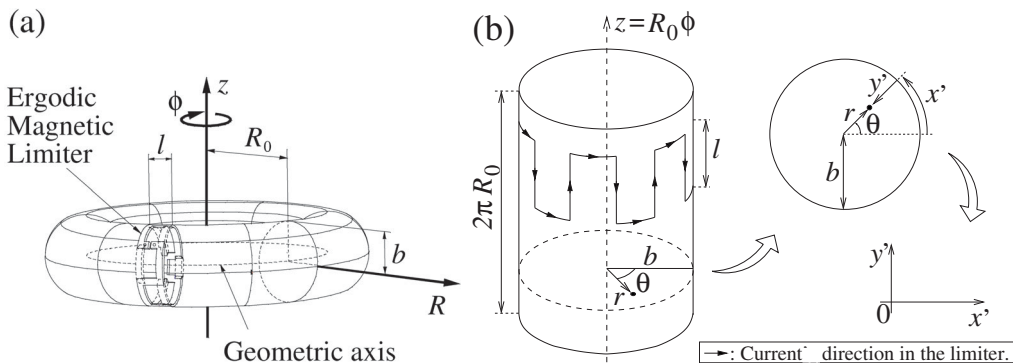
Fig. 1. Schematic view of (a) the tokamak toroidal chamber and the ergodic limiter configuration; (b) the periodic cylinder approximation and the rectangular coordinates used to describe field lines.

since the structure of the field lines in a tokamak is Hamiltonian, magnetic field lines can be more easily appreciated by examining a return map. In such a map the time-like coordinate is the toroidal angle, hence the return map is on the Poincaré surface of section defined by the plane $z = \text{const}$. We let (r_n, θ_n) [or (x_n, y_n)] be the coordinates of the n-th piercing of a given field line with that surface, and take them as our map variables. The field line map is written, in a general form, as $r_{n+1} = f(r_n, \theta_n)$, $\theta_{n+1} = g(r_n, \theta_n)$, where f and g depend on the magnetic field components. Due to magnetic flux conservation, it is necessary that the map be symplectic, so as to preserve areas in the Poincaré surface of section.

The *winding number*, also known as *rotational transform*, and denoted by ι, is defined as $\iota \equiv 2\pi \langle d\theta/d\phi \rangle$, and is the pitch angle of the helical field lines on the magnetic surfaces, which can be numerically calculated along an orbit by $\iota = \lim_{n\to\infty}(\theta_n - \theta_0)/n$. The winding number is most commonly used in nonlinear dynamics texts, while the *safety factor*, $q = 2\pi/\iota$, is more often found the in plasma physics literature. The dependence of the equilibrium safety factor q_{eq} on the radius is dictated by the details of the equilibrium magnetic field, which in turn depend also on the toroidal plasma current. An important quantity is the so-called *magnetic shear*, which is proportional to the derivative of the safety factor with respect to the radius.

Let the equilibrium magnetic field of a tokamak, in the cylindrical approximation, be $\mathbf{B}^0 = (0, B_\theta^0(r), B_T)$. The magnetic field line equations give $dr/d\phi = 0$, such that a field line lies on a surface of constant radius. On integrating the remaining equation between two successive piercings of a magnetic field line with the Poincaré surface of section, one obtains,

$$r_{n+1} = r_n, \tag{1}$$
$$\theta_{n+1} = \theta_n + \iota(r_{n+1}) \pmod{2\pi}, \tag{2}$$

which is written using r_{n+1} (instead of r_n) in the right-hand side in order to put Eqs. (1)–(2) into the form of a canonical transformation, such that the map equations can be obtained from a second-order generating function $F_2 = F_2(r_{n+1}, \theta_n)$ as $r_n = \partial F_2/\partial\theta_n$ and $\theta_{n+1} = \partial F_2/\partial r_{n+1}$, where $F_2(r_{n+1}, \theta_n) = r_{n+1}\theta_n + \int^{r_{n+1}} \iota(r')\mathrm{d}r'$.

A rational value of $\iota/2\pi$, say M/N, gives origin to a periodic orbit of period N of the map (1)-(1), $\theta_{n+N} = \theta_n + 2\pi M$, i.e., a field line closes on itself after N toroidal revolutions and M complete poloidal turns. An irrational value of $\iota/2\pi$ leads to a quasi-periodic orbit, which densely fills the magnetic surface. This map is the prototype of an equilibrium configuration of a tokamak, that can subsequently be perturbed by a second map. From Hamiltonian dynamics, such periodic orbits resonate with the perturbation, yielding pendular shaped islands [10].

When the safety factor is a monotonic function of the radius (i.e., the shear is nonzero everywhere), the map is said to be *twist*. On the other hand, when q has an extreme for example, the map is called *non twist* [11–13]. Thus a map is twist if initial conditions on increasing radius, on a fixed poloidal position, display only increasing (or only decreasing) values of ι, being nontwist otherwise. In terms of the map (1) the twist condition means that the derivative $\partial\theta_{n+1}/\partial r_n = \partial\iota(r_{n+1})\partial r_n$ does not change sign over the possible values of r_n. In tokamaks, non twist profiles may result from hollow toroidal current profiles (i.e., displaying low current density close to the column center), which can be obtained by many experimental techniques and are related to enhanced confinement; for example when neutral beam injection is applied [14–17]. For twist maps, according to KAM theory, most quasi-periodic orbits (called invariant curves in the surface of section) survive to perturbations weak enough [10]. The non monotonic safety factor profile has a major influence on the trajectories topology, leading to scenarios where increasing perturbation strength causes islands in non twist region to interact in a different way from islands observed in twist maps [18].

3 Standard twist and non-twist maps

The Chirikov-Taylor standard map has been widely used for studying fundamental properties of Hamiltonian systems [19, 20]. It is a radial twist map, given by the equations,

$$r_{n+1} = r_n + K\sin(\theta_n), \tag{3}$$
$$\theta_{n+1} = \theta_n + r_{n+1} \pmod{2\pi}, \tag{4}$$

where K quantifies the strength of the perturbation acting on the radial variable. Let a general magnetostatic perturbation of the form $\mathbf{B}^1 = (B_r^1(r,\theta,\phi), B_\theta^1(r,\theta,\phi), B_\phi^1(r,\theta,\phi))$. Assuming that $|B_\phi^1| \ll |B_T|$. Supposing also that B_θ^1 is much smaller than the equilibrium toroidal field, and integrating the field line equations over a complete turn on the torus we obtain,

$$r_{n+1} = r_n + \frac{R_0}{B_T} \int_0^{2\pi} B_r^1(r_{n+1}, \theta_n, \phi) \mathrm{d}\phi, \qquad \theta_{n+1} = \theta_n + \iota(r_{n+1}). \tag{5}$$

The standard map can be obtained by considering a highly idealized situation for which only one mode of the perturbed radial field (taken also to be independent of r) is retained, $(R_0/B_T) \times \int_0^{2\pi} B_r^1(\theta_n, \phi)\mathrm{d}\phi \equiv K\sin(\theta_n)$, and the following monotonic safety factor profile is considered: $q(r) = 2\pi/r$, which corresponds to $\iota(r_{n+1}) = r_{n+1}$. In this case the twist condition is fulfilled, and the corresponding generating function is $F_2(r_{n+1}, \theta_n) = r_{n+1}^2/2 + r_{n+1}\theta_n + K\cos(\theta_n)$.

For these reasons, although the standard map models highly idealized tokamak magnetic fields, it is still used because it has the same fundamental properties of more complicated maps, and moreover it gives us valuable insights on the magnetic field line diffusion [21]. Many basic results obtained for the standard map remain valid for the whole class of twist maps. The standard map is also particularly useful as a description of the local dynamics of more complex maps [10]. One of the general phenomena for which the standard map already gives an overall explanation is the effect of resonant perturbation onto the previously integrable dynamics, with the raising and growth of islands and surviving invariant tori, as described by the Poincaré-Birkhoff and Kolmogorov-Arnold-Moser theorems [10]. Another important phenomenon is the onset of global chaos in phase-space through the interaction of nearby resonances, the invariant tori and islands being destroyed with increasing perturbation.

For $K < K_C \approx 0.971635406/2\pi$, there are still some surviving Kolmogorov-Arnold-Moser tori between the islands, the last one being the torus with rotation number equal to the golden mean. These tori act as barriers that limit the radial diffusion of field lines. Such a large-scale diffusion is enhanced by the accelerator modes, which exist due to the double periodicity of the standard map. From now on, we shall write the standard map in the following form, for further comparisons with more complicated models, using $x = \theta/2\pi$ and $k \equiv 2\pi K$:

$$y_{n+1} = y_n + (k/2\pi)\sin(2\pi x_n), \tag{6}$$
$$x_{n+1} = x_n + y_{n+1} \pmod 1. \tag{7}$$

Playing, among the non twist systems, a similar role as the standard map for twist systems, the standard non twist map has a more recent history, but has been already extensively studied [22,23] and references therein. The standard non twist map breaks the twist condition by displaying a quadratic safety factor profile, such that $\iota(r)$ has a local minimum at some radius (called "shearless radius"). It is usually written in the following form

$$y_{n+1} = y_n - b\sin(2\pi x_n), \tag{8}$$
$$x_{n+1} = x_n + a(1 - y_{n+1}^2) \pmod 1, \tag{9}$$

where b measures the perturbation strength, just like in the standard map, and a is a winding number profile parameter. In the same way as the standard map, the standard non-twist map may appear as a local approximation of more complicated non-twist maps [24,25]. The non twist standard map appears in tokamak models for which the safety factor profile is non-monotonic. This is the case, for example, in the first stages of the plasma discharge where the plasma column is hollow; and also as a result of non-inductive current drive like neutral beam injection. Many important results, such as the KAM theorem, hold only for twist systems. Indeed, the standard non twist map presents new phenomena, such as the presence of two island chains of the same period at opposite senses of the shearless radius. These islands, as the perturbation becomes stronger, approach each other with reconnection of their separatrices instead of the island erosion through tori destruction which is characteristic of the Chirikov overlapping scenario that holds for twist maps [22]. The reconnection processes are mainly of two types: (i) homoclinic, where the island centers are vertically aligned; (ii) heteroclinic (or
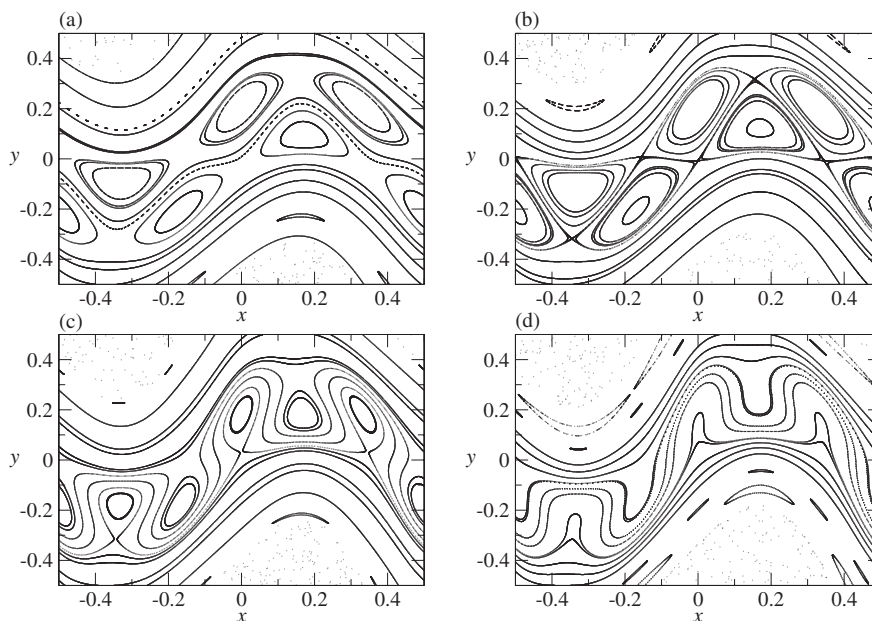
Fig. 2. Phase portraits depicting the reconnection process in the standard non-twist map for $a = 0.345$ and (a) $b = 0.35$; (b) $b = 0.376072$; (c) $b = 0.42$; (d) $b = 0.461434$ [26].

loop reconnection), where the island centers are counter-aligned, i.e., with elliptic points of one island chain aligned with hyperbolic points of the other.

The basic process of the heteroclinic is displayed in Fig. 2: the non monotonic safety factor profile leads to the existence of pairs of tori with the same q, therefore a resonant perturbation gives rise to two island chains with the same period, separated by invariant curves (Fig. 2(a)). As the perturbation increases, the islands widths grow and their separatrices merge into a connected curve (Fig. 2(b)). For higher values of the perturbation strength the island chains interchange the separatrix trajectories that connect the hyperbolic points, creating a loop configuration (Fig. 2(c)). For a perturbation strength large enough there is a saddle-center bifurcation where the island chains disappear as their elliptic and hyperbolic points collide. For even higher perturbations, there remains an invariant barrier separating the regions in the phase space where the islands were located before the bifurcation Fig. (2(d)).

The standard non twist map also exhibits the homoclinic reconnection scenario, that leads to the so-called vortex or dipole topology where, as a parameter varies, the vertically aligned hyperbolic points meet the invariant curve between the chains and then move on the invariant curve until they collide together with the elliptic points of the chains. Other reconnection scenarios have also been observed for the standard non twist map [27, 28]. Only (asymmetric) loops and vortex pairs are thought to be generic [29], as well as the vortex pair reconnection, or *tripling reconnection*, which involves the creation of a third island chain as well as a loop [30]. The loop reconnection is associated with the appearance of invariant curves that are not graphs over the x axis, the so-called *meanders*. The existence of these meanders between the reconnected island chains in the standard non twist map has an important consequence on the transport properties of a tokamak, given that it acts as a transport barrier [23, 27, 31, 32]. However, local diffusion is found to be enhanced as reconnection processes occur [18, 33].

4 Ergodic limiter maps

The Martin-Taylor map [9] was one of the first maps designed to model magnetic field lines in tokamaks and the first to consider the effect of an ergodic magnetic limiter. The latter is an
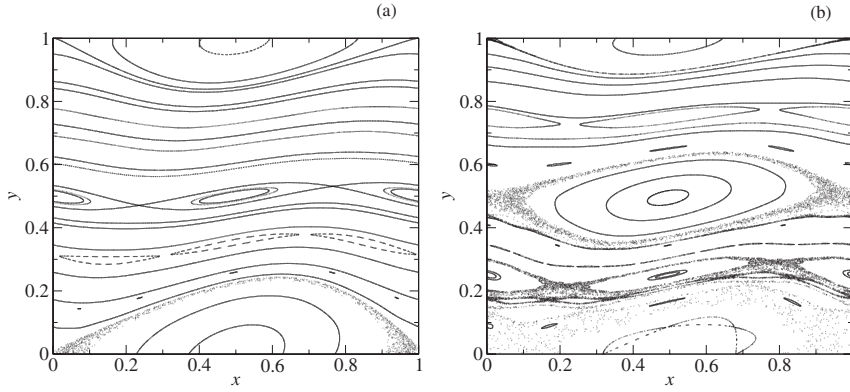
Fig. 3. Phase portraits of the Martin-Taylor map for (a) $s = 2\pi$, $p = 0.1$; (b) $s = 4\pi$, $p = 0.1$.

arrangement of currents external to the plasma, which creates a perturbing magnetic field which is stronger in the vicinity of the tokamak wall. Hence the perturbation resonates chiefly with rational flux surfaces near to the wall, yielding a peripheral region of chaotic magnetic field lines, with the purpose of controlling plasma-wall interactions. It was thought, at first, that a chaotic field line layer could uniformize diffusion in the tokamak edge, thus distributing the heat and particle loading on the tokamak wall in a more uniform way, so diminishing plasma contamination through sputtering and other related processes. It turns out that this is not quite the case, since the chaotic region itself is not homogeneous, and the loadings are not uniform, but rather present magnetic footprints with a complicated (actually fractal) nature.

The Martin-Taylor map consists of the composition of two maps: an integrable map for the equilibrium dynamics and a symmetry-breaking perturbative map. The equilibrium part, M_1, is a simple twist map, its orbits keeping a fixed radius (y), while the angular (x) advance per iteration varies linearly with the radius. This is similar to what happens with the standard map, but now with the introduction of a magnetic shear parameter, s, defined as the radial derivative of the safety factor, calculated at the plasma edge. The perturbative map, M_2, models the ergodic magnetic limiter action and is obtained from the calculation of the magnetic field generated by a current ring mounted over the tokamak vessel. The current ring is represented by a ring-shaped coil with pairs of straight segments oriented along the toroidal direction, with currents flowing in opposite senses for adjacent segments, as depicted in Fig. 1. The limiter is supposed to act only on the thin toroidal section it occupies, the rest of the torus being characterized only by the the equilibrium field. The composition of these two maps, $\mathsf{M} = \mathsf{M}_1 \circ \mathsf{M}_2$, gives the following equations:

$$x_{n+1} = x_n + sy_n + g(x_n, y_n) \pmod{2\pi}, \tag{10}$$

$$y_{n+1} = y_n + h(x_n, y_n), \tag{11}$$

$$g(x, y) = -pe^{-y}\cos x + sh(x, y), \tag{12}$$

$$h(x, y) = \ln\left|\cos(x - pe^{-y}\cos x)\right| - \ln\left|\cos x\right|, \tag{13}$$

where the parameter p quantifies the perturbation strength, proportional to the current in the limiter coils. This is an area-preserving map, but it is not written in terms of a second kind generating function, as is the standard map.

The effect of the changing the map parameters p and s is exemplified in Fig. 3, where we depict a phase portrait for weak perturbation, showing the formation of a narrow chaotic field line layer near the tokamak wall (Fig. 3(a)). Doubling the magnetic shear causes this layer to enlarge substantially (Fig. 3(b)). The causes of this enlargement are distinct, though, for increasing p makes the island grow, whereas increasing the magnetic shear bring the islands closer to each other more than it decreases their size, as also observed for a stellarator model [34]. The Martin-Taylor map satisfies the conditions for a tokamak map proposed by Balescu [35]: it has a realistic safety factor profile, in the sense that s can be chosen appropriately, and

its orbits are always bounded towards $y = 0$, whose location is left free in the model. Analytical approximate results, based on the Chirikov criterion of island overlapping [10], can be obtained for the onset of global chaos and the size of the chaotic region in the Martin-Taylor map [9], with good agreement with numerical simulations, despite the unequal widths of the islands, the deviations observed between analytical and numerical results being the results of our neglecting higher-order island interactions in the perturbative treatment [36]. The transport properties of the Martin-Taylor map have also been determined, the radial diffusion of field lines in the chaotic region being anomalous, initially displaying approximately diffusive behavior, and followed by a decrease caused by field line losses due to their collisions with the tokamak wall.

The Ullmann map [37] models the magnetic fields in a tokamak with an ergodic limiter, using a second kind generating function, and it is based on a previous map [38]. Its advantage over the Martin-Taylor map are the use of parameters more closely related to physically measured quantities (like the safety factor and limiter current) and the consideration of toroidal effects. In addition, the Ullmann map satisfies the conditions for a tokamak model outlined in [35]. The Ullmann map is given as a composition of two maps – the equilibrium map

$$r_{n+1} = \frac{r_n}{1 - a_1 \sin \theta_n}, \tag{14}$$

$$\theta_{n+1} = \theta_n + \frac{2\pi}{q_{\text{eq}}(r_{n+1})} + a_1 \cos \theta_n \pmod{2\pi}, \tag{15}$$

and the perturbation map

$$r_n = r_{n+1} + \frac{mC\epsilon b}{m-1} \left(\frac{r_{n+1}}{b} \right)^{m-1} \sin(m\theta_n), \tag{16}$$

$$\theta_{n+1} = \theta_n - C\epsilon \left(\frac{r_{n+1}}{b} \right)^{m-2} \cos(m\theta_n), \tag{17}$$

where the parameter a_1 gives the strength of the toroidal correction to the periodic cylindrical equilibrium, and ϵ is proportional to the current in the limiter and quantifies the perturbation strength due to the magnetic ergodic limiter, m is the number of pairs of toroidal current ring segments, b is the tokamak minor radius, and C is a geometrical factor [25].

The equilibrium part requires the specification of a safety factor monotonic profile [37,39]. Since the Ullmann map is intended to study the tokamak edge, it is convenient to show phase portraits using the normalized rectangular coordinates, $y = 1 - r/b$ and $x = \theta/2\pi$, so that the tokamak wall lies at $y = 0$, as in the Martin-Taylor map. For a small perturbation strength, as $\epsilon = 0.07$, the monotonic Ullmann map presents a chaotic field line layer at the tokamak edge, and is mostly regular in the remaining of the phase space (Fig. 4(a)). The main results obtained so far using the Ullmann map are related to the escape basins and invariant manifold structure, for the monotonic version of the map [39], and the destruction and transport through the barrier in the non monotonic case to be considered later on [25]. The concept of an *exit* [40, 41] arises naturally in tokamak models, the tokamak wall itself being an exit for the field lines wandering through the chaotic region in the tokamak edge. Other types of exits are material obstacles inside the tokamak, as divertor plates, antennas, and probes, which can be placed inside the tokamak vessel with different purposes. In all cases above a field line is considered lost once it reaches the considered exit.

The *escape basin* related to a given exit is the set of initial conditions (in the Poincaré surface of section) which generates field lines that eventually hit that exit after some number of map iterations. The exits are usually set in the outer region of the tokamak, where obstacles are more likely to be found. Since this region is also typically characterized by chaotic field lines (specially if there is an ergodic limiter), we expect escape basins to have a complicated structure due to the intricacies of the manifold structure. The exit basins can be numerically obtained by iterating a grid of initial conditions in the phase plane and plotting them according to the exit at which the field line have hit. As an example, let us consider a rectangular exit
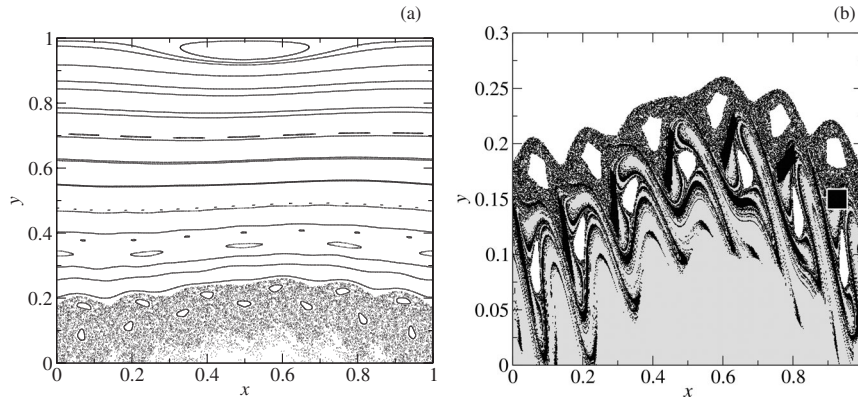
Fig. 4. (a) Phase portrait for the Ullmann map, with $m = 7$ and $\epsilon = 0.07$. (b) Exit basins of the Ullmann map for orbits escaping through the wall at $y = 0$ (gray pixels), and a rectangular exit $w_y = 0.0182$, $w_x = 10w_y/\pi$ (black pixels), for $m = 7$ and $\epsilon = 0.07$. White pixels represent field lines which do not either hit the wall or the rectangular exit.
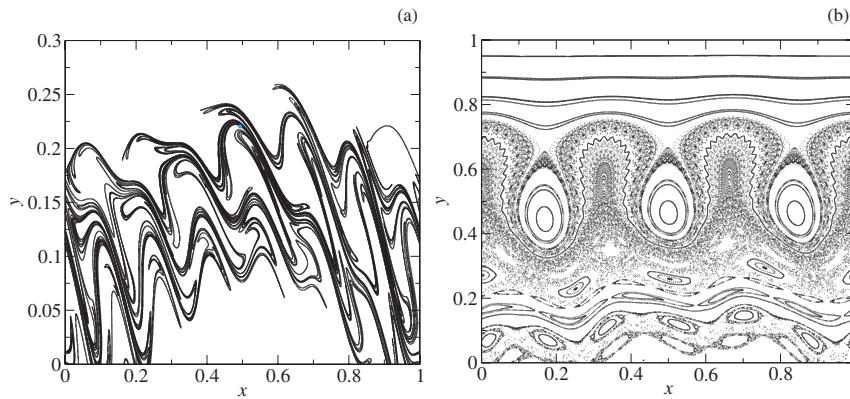
Fig. 5. (a) Ullmann map phase portrait depicting a finite-length approximation of the stable manifold in the chaotic field line region, with $m = 7$ and $\epsilon = 0.07$. (b) Phase portrait for the non-twist Ullmann map for $\epsilon = 0.3$. The transport barrier is the rippled line meandering around the main islands.

placed inside the chaotic outer region of the phase portrait depicted by Fig. 4(b). Black pixels represent initial conditions generating field lines that hit the rectangular exit, and gray pixels are for field lines that hit the wall at $y = 0$.

The exit basins have an involved, and actually fractal structure. The nature of the basin boundaries is determined by the invariant manifolds of the unstable periodic orbits embedded in the chaotic layer. In the latter there is an infinite but countable number of saddle points, of all periods, and their invariant stable and unstable manifolds constitute a foliation of the chaotic sea [42]. Let us consider the inverse images, under the action of the Ullmann map, of the rectangular exit depicted in Fig. 4(b): it expands in one direction and shrinks along the other direction (due to the area-preserving property of the map). Such directions are provided by the unstable and stable manifolds, respectively, of unstable periodic orbits embedded in the chaotic region [42]. Chaotic trajectories are repelled along the unstable manifolds of such orbits. In Fig. 4(b) the increasingly distorted rectangles to the left of the rectangular exit are inverse images of it which do not cross the other exit. Hence these inverse images belong to the corresponding exit basin. Thus, iterating backwards the exit region is, discarding orbits that hit the wall, a way of obtaining a numerical approximation to the exit basin. The exit basin boundary can be calculated in a similar fashion by iterating backwards the points of the exit boundary (shown in white in Fig. 4(b)). Figure 5(a) displays a
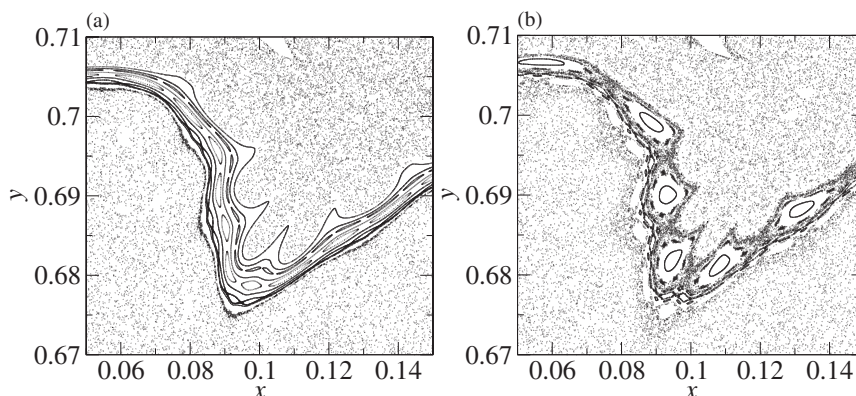
Fig. 6. Zoom near the barrier for the non-twist Ullmann map for (a) $\epsilon = 0.3029$ and (b) $\epsilon = 0.3031$.

finite-length approximation of the stable manifolds, obtained by iterating 60 times backwards a large number ($\sim 10^7$) of initial conditions located in the chaotic region, the result being compatible with the exit basin boundary depicted in Fig. 4(b).

The Ullmann map becomes a non-twist one by considering a non-monotonic equilibrium safety factor profile [43]. The resulting non-twist Ullmann map has properties similar to the standard non-twist map, as illustrated in Fig. 5(b), where an invariant barrier meanders around the remaining island chain after the reconnection and bifurcation, which is the same situation depicted in Fig. 2. There are, however, two main differences between the phase portraits of the standard non twist map and the non monotonic version of the Ullmann map. The first difference is that the asymmetry of the perturbation term in the non-monotonic Ullmann map produces a wider chaotic layer below the barrier than above it. The second difference is the presence of invariant curves outside the shearless region close to the wall, which is possible due to the localized nature of a resonant perturbation.

The perturbation strength necessary for destroying the invariant barrier, ϵ_c, is numerically determined by first considering whether or not a given field line has crossed it after a large number of iterations, which sets up an upper bound for the critical value. Secondly we vary ϵ and seek a field line that maps out an invariant curve at the barrier location, thus setting a lower bound to ϵ_c. Repeated application of this procedure leads to the value $\epsilon_c \approx 0.30303$ for the non-twist Ullmann map, which was considered in Fig. 6. Even after the destruction of the invariant barrier an effective transport barrier persists, due to the stickiness of field lines around the many island chains present in the chaotic region. By *stickiness* we mean that, whenever there are periodic islands embedded in the chaotic sea, field lines spend a typically large number of map iterations encircling those islands before they eventually go away from them. If the chaotic region intercepts the tokamak wall, it turns out that the field lines escape after a given time (measured in number of map iterations). For perturbation values slightly above ϵ_c the loss of field lines along the radial direction is found to occur at an exponential rate. Let us consider an ensemble of initial conditions randomly distributed over the chaotic region above the barrier. The fraction F_n of the field lines that remain in that region at the n-th iteration decays as $e^{-\beta n}$, where $\beta \approx 1.4 \times 10^{-5}$ is the escape rate determined for the non-twist Ullmann map. This exponential scaling holds for the first hundreds of thousands of iterations, after which F_n decays in a power-law fashion. We observed that, similarly to the standard non-twist map [44], the transport in the non-twist Ullmann map is diffusive, i.e., the mean quadratic radial deviation of field lines increases linearly with the number of iterations. The local expansion of the twist Ullmann map around a given radius yields the standard map with an additional perturbation term, a system already studied in the context of the break up of invariant golden tori [45]. Such an expansion for the non-twist Ullmann map similarly consists of the standard non-twist map with a symmetry-breaking additional perturbation term [13] arising from the toroidal correction [25].
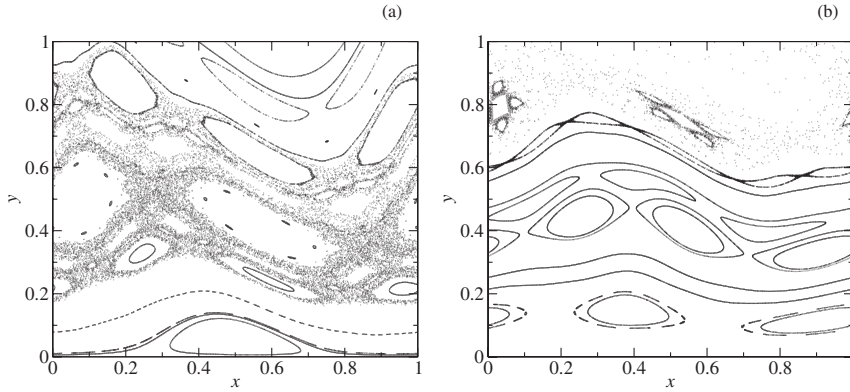
Fig. 7. (a) Phase portrait of the tokamap for $k = 4$ and $w = 1$. (b) Phase portrait of the revtokamap with $k = 4$, $\iota_0 = 1/3$, $\iota_{\max} = 2/3$, and $\iota_1 = 1/6$.

5 Balescu maps

In the late 90's, Balescu and collaborators have proposed a field line map (*tokamap*) [35] that, although not directly derived from magnetic field equations, represent the global field line dynamics in a tokamak. It is derived from a modified version of the generating function for a stellarator subject to a localized perturbation [34]. The tokamap equations are

$$y_{n+1} = \frac{1}{2} \left\{ P(x_n, y_n) + \sqrt{[P(x_n, y_n)]^2 + 4y_n} \right\}, \tag{18}$$

$$x_{n+1} = x_n + \iota(y_{n+1}) - \frac{k}{(2\pi)^2} \frac{1}{(1 + y_{n+1})^2} \cos(2\pi x_n) \pmod 1, \tag{19}$$

with $P(x, y) = y - 1 - (k/2\pi) \sin(2\pi x)$, where k is the perturbation strength and ι is the winding number. The winding number profile adopted, for a cylindrical description, is $\iota(y) = (\iota_0/4)(2 - y)(2 - 2y + y^2)$, where $\iota_0 = 1/q(0)$ is the winding number value on the magnetic axis.

In this case the radial variable y is measured from the magnetic axis, instead of the tokamak wall, as in the Martin-Taylor and Ullmann maps. The tokamap was designed to meet some desirable properties: (i) the avoidance of negative values of y, i.e. with $y_0 = 0$ implying $y_n \geq 0$ for all n; and (ii) the use of a realistic winding number profile. Figure 7(a) shows a phase portrait of the tokamap for typical parameter values, $k = 4$ and $\iota_0 = 1$, displaying a well-developed chaotic region still bounded by invariant tori. The wall position is left free in the tokamap model. The radial transport properties of the tokamap are similar to those obtained for the twist standard map with non-global chaos, where the existence of the KAM curves bounding the chaotic layer and sticking regions around islands leads to a sub-diffusive transport regime [35]. The stickiness phenomenon associated with the embedded islands also results in intermittent behavior, allowing a statistical description of diffusion by means of random walk models [46]. The most resistant tori to perturbation are those with noble winding numbers and found close to the main islands, just as in the standard map [47,48], agreeing with experimental observations and theoretical considerations [34]. An extensive account of the transport and the noble barriers in the tokamap can be found in [49], and a more recent study of the barriers in [50]. A closely related model, which preserves the symplectic structure and is obtained from a Hamiltonian valid for vanishing perturbation [51], results in a kind of symmetric tokamap [52]. The symmetric tokamap turns out to be more resistant to the perturbation than the non-symmetric version and the order in which the KAM curves are destroyed is also different. Nevertheless the transport properties are found to be the same for both symmetric and non-symmetric models; similar remarks being true also for the revtokamap [53].

The freedom in the choice of the winding number profile allows us the use the tokamap to study non-twist regimes by simply changing the profile to a non-monotonic one, like

$\iota(y) = \iota_{\max}\left[1 - a(cy - 1)^2\right]$, where $\iota_{\max}$ is the maximum of $\iota(y)$ and the parameters a and c can be written in terms of the winding number values at two given positions, namely $\iota_0 \equiv \iota(y = 0)$ and $\iota_1 = \iota(y = 1)$: $a = (\iota_{\max} - \iota_0)/(\iota_{\max})$ and $c = 1 + [(\iota_{\max} - \iota_1)/(\iota_{\max} - \iota_0)]^{1/2}$. Equations (18)–(19), with this profile have been called the *revtokamap* [54]. Typical values for these constants are approximately $\iota_0 = 1/3$, $\iota_{\max} = 2/3$, and $\iota_1 = 1/6$. Small variations in these parameters can lead to significant changes in the phase space configuration. Considering these values, and $k = 4$, Fig. 7(b) show some orbits before the loop reconnection process. A comprehensive study of the fixed points for the revtokamap can be found in [54], where it was considered an extended phase space that includes the regions outside the physical range $0 < y < 1$. In the same way as for the tokamap, a (kind of) symmetric revtokamap can be constructed [53], with similar results holding for the symmetric versions of both the tokamap and the revtokamap.

6 Divertor maps

A divertor is a magnetic configuration created by electric currents placed externally to the tokamak, such that the field lines have escape channels, through which plasma particles can be diverted out of the tokamak wall and redirected to divertor plates, in order to control the plasma impurity content [5,7,55]. Divertors work chiefly due to the chiefly chaotic magnetic field line region near the tokamak wall, where divertor plates are usually placed. Hence field line maps are widely used in the plasma literature to model and predict divertor properties.

The simple divertor map has been presented as the simplest model for the magnetic configuration of a tokamak equipped with a divertor. The simple divertor map is particularly intended for studying the magnetic flux and footprints on the divertor plates [56]. The so-called *magnetic footprints* are the sets of points where the field lines strike those plates. The magnetic footprints on a divertor reflect the underlying dynamical structure of the chaotic field line layer, namely the homoclinic tangle of invariant manifolds which act as fast escape channels for the trajectories. Hence the footprints are traces of the invariant manifolds as they hit the divertor plates. Since the structure of the homoclinic tangle is self-similar we expect magnetic footprints to have a fractal nature, which actually has been confirmed experimentally [57].

The simple divertor map is given by the following equations:

$$x_{n+1} = x_n - k y_n (1 - y_n), \tag{20}$$
$$y_{n+1} = y_n + k x_{n+1}, \tag{21}$$

where (x_n, y_n) are the rectangular coordinates on the poloidal surface of section and the parameter k determines both the safety factor and the strength of toroidal asymmetries in the magnetic field, either natural or externally imposed. Indeed, the perturbation term in Eq. (20) is ky^2, and the safety factor per iteration, in the linearized system, denoted as q_1 is given by the solution of the following transcendental equation $\sin(2\pi/q_1) = k(1 - k^2/4)^{1/2}$. We added to the map a parameter, N_{map}, which is the number of iterations equivalent to one toroidal turn, introduced in order to yield a realistic safety factor profile. As an example, for $k = 0.6$, there results $q_{1\,\mathrm{axis}} \approx 10$ and $q_{1\,\mathrm{edge}} \approx 30$, so that $N_{\mathrm{map}} = 10$ renders $q_{\mathrm{axis}} \approx 1$ and $q_{\mathrm{edge}} \approx 3$.

The strike points of the magnetic field lines on the divertor plates, which generate the magnetic footprints, may not be clearly determined from the simple divertor map, due to the discreteness of map iterations. A more accurate determination of the strike points would come from turning the time-like variable n into a continuous variable φ, which can be thought as a parameterization of the field line. The simple divertor map is then written in the form

$$x(\varphi) = x_n - k\varphi y_n(1 - y_n), \tag{22}$$
$$y(\varphi) = y_n + k\varphi x(\varphi), \tag{23}$$

where $\varphi \equiv N_{\mathrm{map}}\phi/2\pi$ acts as the linear *weight* of the parameter k from the n-th to the $n{+}1$-th iteration, so that $(x(0), y(0)) = (x_n, y_n)$ and $(x(1), y(1)) = (x_{n+1}, y_{n+1})$.

Another advantage of making the time-like variable a continuous one is that the simple divertor map can now be obtained as an approximate solution of the canonical equations from
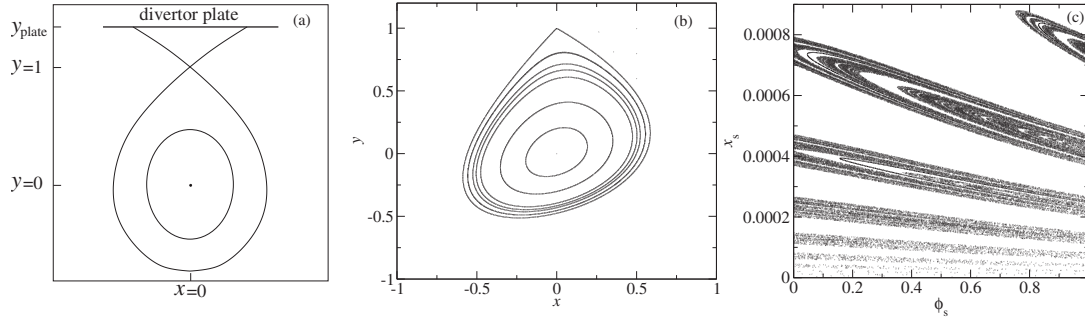
Fig. 8. (a) Schematic view of a divertor equilibrium configuration. (b) Phase portrait and (c) magnetic footprint for the simple divertor map with $k = 0.6$.

the integrable Hamiltonian $H(x, y) = kx^2/2 + (k/3)(y^2 - y^3)$, with φ being the time-like variable, x the canonical momentum, and y the canonical position. The mechanical equivalent of this hamiltonian is a particle subjected to a one-dimensional potential function $U \propto y^2/2 - y^3/3$ for which $U(y \to \pm\infty) \to \mp\infty$, with a well encircling $y = 0$ and a hill around $y = 1$. The phase portrait corresponding to the equilibrium situation described by the continuous simple divertor map is depicted in Fig. 8(a): the divertor plate is placed at $y = y_{plate}$ and in a symmetric way with respect to the x coordinate. There are closed curves encircling the elliptic point at $(0, 0)$ corresponding to stable oscillations of the particle in the potential well in the mechanical equivalent, or the closed flux surfaces which contain the plasma in the tokamak. The hyperbolic point at $(0, 1)$ is the unstable equilibrium point at the top of the potential local maximum, whose manifolds form a closed loop at one side and two open branches at the other side, ending on the divertor plate. The continuous system of Eqs. (22)–(23) is integrable but, if we discretize the time-like variable to obtain the simple divertor map, chaotic dynamics would be possible. Hence the divertor map has a thin layer of chaotic field lines at the region occupied by the separatrix connecting the elliptic and hyperbolic points. Particles reaching this chaotic layer would be thus diverted to the plate due to the chaotic transport along the layer. A typical phase portrait of the simple divertor map (for weak perturbation) can be seen in Fig. 8(b) which shows KAM tori surrounding the elliptic point in $(0, 0)$, one of them close to the hyperbolic point on $(0, 1)$, in accordance with the continuous description just given.

The procedure for determining the points corresponding to the collisions between field lines and the divertor plates is the following [58]: for a given set of initial conditions and a fixed plate position y_{plate}, one iterates the map until the condition $y_n \leq y_{plate} \leq y_{n+1}$ is fulfilled; then the toroidal location φ_s of the strike point is determined through Eqs. (22)-(23): $y_{plate} = y_n + k\varphi_s[x_n - k\varphi_s y_n(1 - y_n)]$, and the x coordinate of the strike point, x_s, from Eq. (22), is $x_s = x(\varphi_s) = x_n - k\varphi_s y_n(1 - y_n)$. The magnetic footprint obtained by using this routine, considering the simple divertor map with $y_{plate} = 1$ and $k = 0.6$, consists of a set of thin stripes with an involved (actually fractal) structure (Fig. 8(c)). It has a smooth longitudinal structure with a cross-section given by a Cantor-like fractal set, with box-counting dimension $1 + D_C$, where $0 < D_C < 1$. The stripes width increases with k, but without essential structure and shape changes [58]. Considering the "open" field lines, coming from and arriving at the divertor plates, we see that the stochastic orbits quickly collide with the plates. These orbits complete an integer number of poloidal turns, and the area of the footprint generated by the field lines tracing N_p turns decreases quadratically with N_p [59].

The region corresponding to the predominantly chaotic field line layer for the simple divertor map can be approximated by a circular ring with outer radius 1 and inner radius $1 - w$, w being the width of the chaotic layer, defined as the distance along the y axis from the outermost intact torus to $y = 1$. The magnetic footprint area can be estimated by considering a rectangular grid on the divertor plate and adding the areas of those rectangles struck by field lines. The relative density of the magnetic flux on the plates then thus can be estimated by the ratio of the chaotic field line region area to the area occupied by the magnetic footprints. One key result obtained with the simple divertor map is that the magnetic flux density on the divertor plates is roughly

six times bigger than the flux in the chaotic layer, for moderate perturbations [56]. Moreover, the width of the chaotic layer, w, increases with k as $k^7/3$ for $k > 0.6$, as we have estimated from the results of [58]. In addition, the footprint area grows even faster with k and, as w goes from 0.01 to 0.1, the magnetic flux density, directly related to the heat flux density, is reduced by 35% [58].

In addition to the introduction of chaos in the system, the discretization of the hamiltonian solution leads to an asymmetry with respect to the y axis (see Fig. 8(b)), while $H(x,y)$ is an even function of x [58]. Another difference to the Hamiltonian case is that, while the latter is time-independent, the phase portraits obtained from Eqs. (22)–(23) show a dependence on φ [58]. This has led to the introduction of the *symmetric simple divertor map* [58], given by:

$$y_{n+1} = y_n + 2kx_n - 2k^2 y_n(1 - y_n), \tag{24}$$
$$x_{n+1} = x_n - ky_n(1 - y_n) - ky_{n+1}(1 - y_{n+1}), \tag{25}$$

which is the composition of the simple divertor map with its inverse with $k \to -k$. Though the symmetric simple divertor map is not as simple as its non-symmetric version, it models in a better way the dynamics of the corresponding Hamiltonian and it is the usual choice as the unperturbed model for the implementations of more sophisticated divertor models [55, 60]. For $k = 0.3$, the choice $N_{\mathrm{map}} = 10$ results in a realistic safety factor profile.

The parameter k affects the symmetric simple divertor map properties differently from the way it does in the simple divertor map, and comparisons between the two maps have to be made carefully. A useful quantity to consider is the width of the chaotic layer, w, which varies with k as $\exp(25k^2)$ for the symmetric simple divertor map. The footprint width increases with k as k^{12}, its structure and shape remaining the same as in the simple divertor map. The fraction of orbits striking the divertor plates decays with the number of poloidal turns as $1/N_{\mathrm{p}}$ [61]. As w goes from 0.01 to 0.1, the magnetic flux density is reduced by 30% [61], which compares well to the value previously found for the simple divertor map. Although the k-dependent terms can simulate general toroidal asymmetries, inherent or external to the model [56], various modified versions of the simple divertor map were introduced to take into account these asymmetries in a more realistic way. Two of these versions that have been recently studied include the so-called low-MN asymmetry, and the effect of a current carrying coil.

The low-MN (or toroidal and poloidal mode) perturbation is introduced in the map as a quadrupole field of toroidal mode number ± 1 [59], which model the unavoidable asymmetries in the equilibrium field obtained in experiments, usually of the order 10^{-4} to 10^{-3} compared to the equilibrium toroidal field [60]. The equations of the symmetric simple divertor map with low-MN perturbation are [60]:

$$y_{n+1} = y_n + 2k(1 - \delta_n)x_n - 2k^2 y_n(1 - \delta_n)(1 - \delta_n - y_n), \tag{26}$$

$$x_{n+1} = x_n - ky_n(1 - \delta_n - y_n) - ky_{n+1}(1 - \delta_n - y_{n+1}), \tag{27}$$

where $\delta_n = \delta_\mathrm{l} \cos(2\pi n/N_{map})$, with δ_l being the amplitude of the low-MN perturbation. The intrinsic perturbation parameter of the map is kept at $k = 0.3$. The width of the chaotic layer increases with the low-MN perturbation as $\delta_\mathrm{l}^{1/2}$, a value predicted by secular perturbation theory [10]. The perturbation causes the phase portraits not to be as symmetric as before, but its main effect, for δ_l in the range $(10^{-4}, 10^{-3})$, is the creation of large islands in the stochastic region. In that range, the fraction Φ of the chaotic flux striking the divertor plates is approximately 75% of the total number of field lines.

As for the simple divertor map [58], the low-MN perturbation reveals itself as a strong factor affecting the footprint properties in the symmetric simple divertor map, with the footprint topology changing from a 10-fold pattern (emerging as a consequence of our choice of $N_{map} = 10$) to a single structure for $\delta_\mathrm{l} \gtrsim 10^{-4}$. For $10^{-4} \leq \delta_\mathrm{l} \leq 10^{-3}$, the footprint area increases from two to four times with respect to its unperturbed value [60]. The average heat flux density on the plates can be estimated as $\Phi A_{\mathrm{sl}}/A_\mathrm{f}l$ where A_{sl} is the area of the predominantly chaotic field line region, A_f is the area of the magnetic footprint, and l is the average orbit length, the latter giving an estimate of the average time it takes for particles from the chaotic layer to reach the divertor plates. From this numerical estimate, the heat deposition is found to increase by a factor of three for $\delta_\mathrm{l} \in (1 \times 10^{-4}, 5 \times 10^{-4})$, then decreasing to 70% of its peak value at $\delta_\mathrm{l} = 10^{-3}$.

Thus, the model assigns a noticeable effect to the small, naturally occurring asymmetries in the toroidal field. Using the density of orbits on the plates to estimate the heat deposition profile on them, it is found, however, that the perturbation makes the heat deposition more homogeneous on the divertor plates [60].

Introduced in [61], the so-called *dipole map* considers a current carrying coil placed on the y axis, with the purpose of investigating the effect of high-MN perturbations on the symmetric simple divertor map equilibrium. The map equations are [55]:

$$x_{n+1} = x_n + 2\delta_d s^3 x_{n+1} \frac{y_n - y_s + s}{[x_{n+1}^2 + (y_n - y_s + s)]^2}, \tag{28}$$

$$y_{n+1} = y_n + \delta_d s^3 x_{n+1} \frac{(y_n - y_s + s)^2 - x_{n+1}^2}{[x_{n+1}^2 + (y_n - y_s + s)]^2}, \tag{29}$$

where s is the distance from the dipole to the last intact torus and δ_{d} is the dipole perturbation strength, proportional to the dipole moment and to $1/s^3$, and normalized by the equilibrium toroidal magnetic field. The dipole perturbation leads to separate chaotic layers in the phase space that result in a composite chaotic layer whose width w increases as $\delta_{\mathrm{d}}^{0.39}$ for $\delta_{\mathrm{d}} \in (0, 6.8 \times 10^{-6})$, and as δ_{d}^8 for $\delta_{\mathrm{d}} \in (6.9 \times 10^{-6}, 7.3 \times 10^{-6})$. There is an abrupt width change, from $w \sim 0.1$ to $w \sim 0.11$, between these ranges, then called pre- and post-transition.

As it happens when k is varied, increasing values of δ_{d} lead to magnetic footprints with the same topology and shape, in contrast to the effect of the low-MN perturbation. There is an increase in the footprint area, but only of about 50% for $\delta_{\mathrm{d}} \in (0, 7.3 \times 10^{-6})$. The fraction of field lines striking the plates decays with the number of poloidal turns as $1/N_{\mathrm{p}}$, regardless of the value of δ_{d}. Moreover, this fraction is reduced to half of its value in the pre-transition range of δ_{d}, and to only 1% of it for $\delta_{\mathrm{d}} = 7.3 \times 10^{-6}$, what is attributed to the predominance of islands in the post-transition range, which reduces the chaotic area and traps part of the chaotic orbits due to the stickiness phenomenon. From the estimate $\Phi A_{\mathrm{sl}}/A_{\mathrm{f}}l$, the average heat deposition is found to decrease moderately (around 17%) with $\delta_{\mathrm{d}} \in (0, 7.3 \times 10^{-6})$. However, using the density of field lines striking the divertor plates, it is found that the dipole perturbation significatively reduces the proportion of hot spots, reducing their number in 75%, as δ_{d} goes from 1×10^{-6} to 7×10^{-6}, while the number of cold and medium spots increases [55].

Other variations of the simple divertor map were also proposed [59]: (i) squaring the parenthesis term in Eq. (20) results in a map that describes a double-null topology; (ii) terms added to the equations leads to a variable ("higher") shear map; and (iii) the simple divertor map composed with a diffuser map, inspired on [9], can model the high-MN perturbations caused by localized coils of ergodic limiters. In order to simulate the plasma particle trajectories, the composition of the simple map with a random non-conservative map was also considered [56,59]. The fine structure of the footprints was then lost and the average width of the footprint was found to increase with the amplitude of the random addition, δ_{R}, as $\delta_{\mathrm{R}}^{1/4}$.

7 Conclusions

In this work we have considered the description of magnetic field lines in tokamaks by means of simple maps. These maps are found to display the same dynamical behavior exhibited by the Hamiltonian equations that describe the tokamak magnetic field lines, despite not being directly derived from these equations in many cases. Each map presented here has its advantages and weaknesses, and the map found most adequate for a certain study depends on the phenomenon that we are describing. Very simple tokamak maps, as the standard twist and non-twist maps, are specially important for giving us the opportunity to study analytically some of the basic dynamical phenomena, and further offering local descriptions of the tokamak dynamics. A global model for the magnetic field in a tokamak is given by the tokamap, which also displays freedom in the choice of the winding number profile. The Martin-Taylor map and Ullmann map describe the tokamak fields in the presence of ergodic magnetic limiters, with the latter also including a toroidal correction. For tokamaks equipped with divertor plates, the simple divertor

map consist in a basic model for the system, to which realistic perturbations are added. As verified for both the simple divertor map and the tokamap, when we attribute a Hamiltonian to a given map (e.g., by showing that the map is an approximate solution to the Hamiltonian), the symmetric version of the map is found to mirror more accurately the dynamics of the corresponding Hamiltonian.

We have considered mapping models [52], construct from magnetic and dynamical considerations to represent the tokamak magnetic field lines behavior. More rigorous methods were developed for obtaining symplectic maps from given Hamiltonians [62–64]. However, to obtain a Hamiltonain appropriate for describing the tokamak dynamics, one would have, e.g., to numerically integrate realistic field lines equations on a grid, with intermediate values being found through interpolation [52]. Further methods for obtaining tokamak maps which can take into account toroidal geometry [65] or other specific consideratoins [66] have been proposed. Simple maps have proven to be an important tool in the study of dynamics of magnetic field lines in tokamaks. Maps require shorter computation times when compared to the numerical integration of the magnetic field line equations-and the simpler they are, the shorter is the time needed for the simulations. We have given examples of such applications in this paper, as the design of the divertor experiments through estimates of the area of the footprints or the heat deposition density, and the quantitative characterization of the anomalous diffusion occurring in the outer tokamak region near its inner wall. Besides this computational advantage, another asset of tokamak simple maps is that analytical treatment can be performed on them, to obtain fixed points, periodic orbits, island widths and so on, using the powerful methods of Hamiltonian dynamics. This analytical treatment allows one to vary the map parameters in order to make realistic choices of parameter values to be used in the design of experiments using, for example, ergodic limiters and divertor plates. We hence conclude that tokamak simple maps are not problems of purely academic interest, being rather a useful tool that provide researchers a deeper understanding of basic physical issues involved in complicated tokamak problems.

References

1. J. Wesson, *Tokamaks* (Oxford University Press, Oxford, 1987)
2. F.W. Perkins, D.E. Post, N.A. Uckan, et al., Nucl. Fusion **39**, 2137 (1999)
3. P.J. Morrison, Phys. Plasmas **7**, 2279 (2000)
4. O. Fischer, W.A. Cooper, Plasma Phys. Rep. **24**, 784 (1998)
5. F. Karger, K. Lackner, Phys. Lett. A **61**, 385 (1977)
6. I.L. Caldas, R.L. Viana, M.S.T. Araujo, et al., Braz. J. Phys. **32**, 980 (2002)
7. T.E. Evans, R.A. Moyer, K.H. Burrell, et al., Nature (Physics) **2**, 419 (2002)
8. M.W. Jakubowski, O. Schmitz, S.S. Abdullaev, S. Brezinsek, K.H. Finken, Phys. Rev. Lett. **96**, 35004 (2006)
9. T.J. Martin, J.B. Taylor, Plasma Phys. Controlled Fusion **26**, 321 (1984)
10. A.J. Lichtenberg, M.A. Lieberman, *Regular and Chaotic Dynamics* (Springer, 1992)
11. R.E. de Carvalho, A.M.O. de Almeida, Phys. Lett. A **162**, 457 (1992)
12. D. del Castillo-Negrete, P.J. Morrison, Phys. Fluids A **5**, 948 (1993)
13. A. Wurm, K. Fuchss, P.J. Morrison, Amer. Phys. Soc. (2006)
14. W. Kerner, H. Tasso, Plasma Phys. Controlled Fusion **24**, 97 (1982)
15. F.M. Levinton, M.C. Zarnstorff, S.H. Batha, M. Bell, R.E. Bell, et al., Phys. Rev. Lett. **75**, 4417 (1995)
16. E.J. Strait, L.L. Lao, M.E. Mauel, B.W. Rice, et al., Phys. Rev. Lett. **75**, 4421 (1995)
17. E. Mazzucato, S.H. Batha, M. Beer, M. Bell, R.E. Bell, et al., Phys. Rev. Lett. **77**, 3145 (1996)
18. G. Corso, F.B. Rizzato, Phys. Rev. **58**, 8013 (1998)
19. J.M. Greene, J. Math. Phys. **20**, 1183 (1979)
20. B.V. Chirikov, Phys. Rep. **52**, 263 (1979)
21. S.S. Abdullaev, K.H. Finken, A. Kaleck, K.H. Spatschek, Phys. Plasmas **5**, 196 (1998)
22. J.E. Howard, S.M. Hohs, Phys. Rev. A **29**, 418 (1984)
23. K. Fuchss, A. Wurms, A. Apte, P.J. Morrison, Chaos **16**, 33120 (2006)
24. W. Horton, H.B. Park, J.M. Kwon, et al., Phys. Plasmas **5**, 3910 (1998)
25. J.S.E. Portela, I.L. Caldas, R.L. Viana, P.J. Morrison, Int. J. Bifur. Chaos **17**, 1589 (2007)

26. A. Wurm, A. Apte, P.J. Morrison, Braz. J. Phys. **34**, 1700 (2004)
27. S. Shinohara, Y. Aizawa, Prog. Theor. Phys. **100**, 219 (1998)
28. A. Wurm, A. Apte, K. Fuchss, P.J. Morrison, Chaos **15**, 23108 (2005)
29. J.E. Howard, J. Humphreys, J. Phys. D **80**, 256 (1995)
30. E. Petrisor, Chaos, Solit. Fract. **14**, 117 (2002)
31. D. del Castillo-Negrete, J. Greene, P.J. Morrison, Physica D **91**, 1 (1996)
32. S. Shinohara, Y. Aizawa, Prog. Theor. Phys. **97**, 379 (1997)
33. S.D. Prado, G. Corso, Physica D **142**, 217 (2000)
34. H. Wobig, Z. Naturforsch. A: Phys. Sci. **42**, 1054 (1987)
35. R. Balescu, M. Vlad, F. Spineanu, Phys. Rev. E **58**, 951 (1998)
36. J.S.E. Portela, R.L. Viana, I.L. Caldas, Physica A **317**, 411 (2003)
37. K. Ullmann, I.L. Caldas, Chaos, Solit. Fract. **11**, 2129 (2000)
38. R.L. Viana, I.L. Caldas, Z. Naturforsch. A: Phys. Sci. **47**, 941 (1992)
39. J.S.E. Portela, I.L. Caldas, R.L. Viana, M.A.F. Sanjuan, Int. J. Bifur. Chaos **17**, 4067 (2007)
40. J. Schneider, T. Tél, Z. Neufeld, Phys. Rev. E **66**, 66218 (2002)
41. M.A.F. Sanjuán, T. Horita, K. Aihara, Chaos **13**, 17 (2003)
42. F. Feudel, A. Witt, M. Gellert, et al., Chaos, Solit. Fract. **24**, 947 (2005)
43. G.A. Oda, I.L. Caldas, Chaos, Solit. Fract. **5**, 15 (1995)
44. G. Corso, A.J. Lichtenberg, Physica D **131**, 1 (1999)
45. J.M. Greene, J. Mao, Nonlinearity **3**, 69 (1990)
46. R. Balescu, Phys. Rev. E **55**, 2465 (1997)
47. J.H. Misguich, Phys. Plasmas **8**, 2132 (2001)
48. J.H. Misguich, J.-D. Reuss, D. Constantinescu, et al., Plas. Phys. Contr. Fus. **44**, L29 (2002)
49. J.H. Misguich, J.-D. Reuss, D. Constantinescu, et al., Ann. Phys. Fr. **28**, 1 (2003)
50. D. Constantinescu, R. Constantinescu, Phys. Scr. T **118**, 244 (2005)
51. M. Eberhard, Phys. Rev. E **71**, 26411 (2005)
52. S.S. Abdullaev, Nucl. Fusion **44**, S12 (2004)
53. A. Wingen, K.H. Spatschek, S.S. Abdullaev, Contr. Plas. Phys. **45**, 500 (2005)
54. R. Balescu, Phys. Rev. E **58**, 3781 (1998)
55. A. Punjabi, H. Ali, A. Boozer, Phys. Plasmas **10**, 3992 (2003)
56. A. Punjabi, A. Verma, A. Boozer, Phys. Rev. Lett. **69**, 3322 (1992)
57. A. Wingen, M. Jakubowski, K.H. Spatschek, S.S. Abdullaev, K.H. Finken, M. Lehen, Phys. Plasmas **14**, 42502 (2007)
58. A. Punjabi, A. Verma, A. Boozer, J. Plas. Phys. **56**, 569 (1996)
59. A. Punjabi, A. Verma, A. Boozer, J. Plas. Phys. **52**, 91 (1994)
60. H. Ali, A. Punjabi, A. Boozer, T. Evans, Phys. Plasmas **11**, 1908 (1994)
61. A. Punjabi, H. Ali, A. Boozer, Phys. Plasmas **4**, 337 (1997)
62. S.S. Abdullaev, J. Phys. A: Math. Gen. **32**, 2745 (1999)
63. S.S. Abdullaev, J. Phys. A: Math. Gen. **35**, 2811 (2002)
64. S.S. Abdullaev, Phys. Rev. E **70**, 46202 (2004)
65. E.C. da Silva, I.L. Caldas, R.L. Viana, Phys. Plasmas **8**, 2855 (2001)
66. R. Barocio, E. Chávez-Alarcón, C. Gutierrez-Tapia, Braz. J. Phys. **36**, 550 (2006)